

Optically Accessible MEMS Resonant Mass Sensor for Biological Applications

Ethan G. Keeler¹, Member, IEEE, Chen Zou¹, and Lih Y. Lin¹, Fellow, IEEE

Abstract—Resonant measurement of mass has emerged as a powerful tool for cellular characterization in biological and medical research. For application in clinical diagnostics and development, in pursuit of large volumes of sample data, microfluidics become an essential conveyor for serial measurement. The nature of channel fabrication within a resonant structure often prohibits optical characterization and manipulation methods within its inner volume due to the opacity of constituent materials. This perpetuates a lost opportunity for simultaneous investigation with important optical techniques, including laser trapping, fluorescent microscopy, flow cytometry, and many other critical approaches. In an attempt to unify these technologies, we seek to maintain the optical availability of samples as they undergo resonant mass measurement. To the best of the authors' knowledge, the resulting device is the first optically-clear fluidic-enabled resonant structure that is scalable for large cellular study. As such, this paper describes the integrated sensor and its supporting system, accompanied by important specifications and metrics. [2018-0278]

Index Terms—Fluorescence, MEMS, microfabrication, microfluidics, optical trapping, resonant sensor, cellular mass sensing.

I. INTRODUCTION

BIOLOGICAL characterization and sensing on the single-cell level have seen impressive development in recent years, questing for insight into fundamental biological and disease processes. As one of the most basic units of life, the cell offers vital information in medical research and therapeutic development. Weight and mass have always been categorizing and observational characteristics for living organisms that reveal important dynamics. Biophysical characteristics at a cellular level can be indicative of human disease or abnormality [1], especially when observing cell growth [2]. For instance, circulating tumor cells in a cancer patient's blood, marking metastatic disease, can indicate overall survival rate in cases of prostate, breast, colorectal, and certain lung cancers; specifically for ovarian cancer, these cells are challenging to

detect with serum markers in early stage illness. Interestingly, these cells present with a decreased dry mass density compared to leukocytes, giving important disease insight [3].

To measure cell size and mass, researchers have employed several approaches, including use of the Coulter counter [4] to determine size and phase-shifting interferometry [5] to optically characterize mass. Micro-electro-mechanical systems (MEMS) emerged as an extremely sensitive platform for detection of the minuscule mass presented by cells, having seen increased attention especially given their high degree of sensitivity and their complementary metal-oxide-semiconductor (CMOS) compatibility [6]. When excited by either thermal fluctuations or external stimulus, these released structures vibrate at a characteristic resonant frequency. This frequency is the product of structural dimensions, material properties, stiffness, and mass. Addition of a sample to the structure perturbs this equilibrium and incites a shift in resonant frequency. Such a shift observes linear tracking for small mass changes and can reveal real-time mass dynamics in a cell; furthermore, mass sensitivity exhibits a linearly proportional relationship with the vibrational amplitude squared [7].

Measurement of dynamic cell mass requires physiological support in a culture media. To this end, Burg *et al.* embedded a fluidic channel within a suspended micro-channel resonator that assumed the form of a cantilever. In this way, the device exhibited high-performance in vacuum, encouraged by a decrease in viscous damping, while simultaneously supporting a fluidic environment for cell growth, culture, and population sampling [8]–[10]. Resonators not only demonstrate a substantial reaction to mass change, but they also respond to the position at which the mass is modulated. As a complication, this positional dependence trickles down to an uncertainty in perceived cell mass and can be exasperated or minimized depending on device topology and a number of factors. Park *et al.* [7] developed a novel resonant pedestal design promising better mass uniformity than observed for cantilever-class devices that supported culture of adherent cell-lines. Such platforms, however, do not provide for easy measurement turnover for necessary statistical sampling, having no integrated microfluidics. Other lines of inquiry have investigated position control within the fluidic channel, as opposed to positional insensitivity, by utilizing mechanical or hydro-dynamic traps [11] or optical trapping [12]. Optical tweezers is very promising for three reasons: it is capable of precise positioning, rapid capture/release, and arbitrary control but requires special consideration for deployment

Manuscript received November 20, 2018; revised February 22, 2019; accepted March 2, 2019. Date of publication April 11, 2019; date of current version May 31, 2019. This work was supported in part by the National Science Foundation (NSF) IDBR Program under Grant DBI-1353718 and in part by the NNCI-Supported Facility under Grant NNCI-1542101. The work of E. G. Keeler was supported by the NSF GRFP, under Grant DGE-1256082. Subject Editor A. Luque. (Corresponding author: Lih Y. Lin.)

The authors are with the Electrical and Computer Engineering Department, University of Washington, Seattle, WA 98195 USA (e-mail: egkeeler@uw.edu; chenzou@uw.edu; lylin@uw.edu).

Color versions of one or more of the figures in this paper are available online at <http://ieeexplore.ieee.org>.

Digital Object Identifier 10.1109/JMEMS.2019.2906586

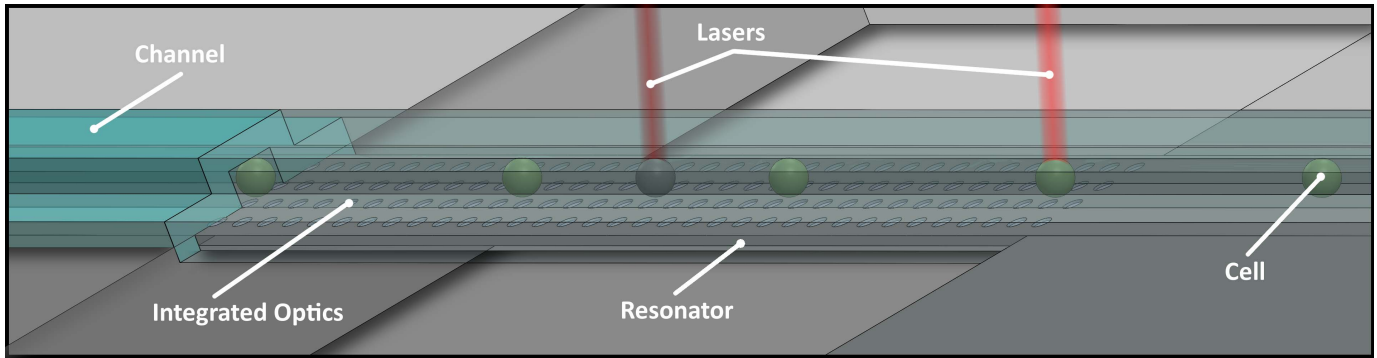


Fig. 1. Device illustration showing the integrated fluidic channel, bridge resonator, external lasers, and sample cells.

with cells. Supported by the work before us and to our best knowledge, we have developed the first cell-enabled platform that integrates optical trapping and optical accessibility with microfluidic-enabled resonant mass sensing for substantiated measurements with cells.

Understanding disease and biological processes necessitates information from a myriad of sources reporting in unison. Furthermore, especially for temporal observation of a cell fixed in place on the structure, simultaneous real-time optical characterizations and mass measurements could greatly inform biological, medical, and pharmaceutical research. Due to the opacity of silicon, typical resonant devices conceal the cell inside of a hollow structure preventing optical probing with key characterization methods, including fluorescent microscopy and flow cytometry, unless expelling the cell from the device. Such structures further prohibit optical manipulation methods. Early devices first sought the capability of biomolecular detection by utilizing a sacrificial polysilicon process to achieve hollow silicon nitride cantilevers ($\sim 1 \mu\text{m}$ channel height) [13], [14]. Silicon nitride is in fact an optically-clear material; however, the employed process is limited in its practical scalability and proves prohibitive when targeting size-scales necessary for cellular research. Secondly, to achieve electrostatic actuation with silicon nitride structures, the deposition of an opaque metal layer is required, further threatening its optical clarity.

Ensuring optical accessibility is not trivial, as it mandates navigation through various trade-offs and obstacles to arrive at a unique approach to fabrication and system design. The device at the center of this work is illustrated by Fig. 1, showing a bridge-resonator that employs an optically clear fluidic channel comprised of transparent parylene-C and a silicon supporting structure. The composite resonator leverages the ideal material properties of single-crystalline silicon and the optical clarity of parylene-C. As a crystalline-amorphous hybrid, it will certainly not rival the performance of pure silicon, but rather offer optical viability as a tradeoff consideration. This dual nature also provides for the integration of optical structures for enhanced trapping [15], in the form of a photonic crystal (PhC). For long-term laser trapping of cells, optical exposure is a grave concern; involvement of a PhC can reduce the required optical intensity for cell trapping and thereby improve their vitality. In this paper, we demonstrate

a device capable of mass measurement that serves as a platform for optical technology integration.

The subsequent section details the fabrication process for these unique structures. The process builds from our previous work [12] by implementing a backside porting approach for more robust and precise fluidic control within the resonator. This is an important improvement for parylene fluidic structures that contrasts with frontside channel access. Implementation of this technique incurred significant fabrication and system improvements to achieve the goal of a platform further optimized for cell mass sensing.

II. DEVICE FABRICATION

Fabrication of a suspended silicon structure is relatively straightforward with silicon-on-insulator (SOI) techniques [16]–[18]; a simple masked dry etch of the device layer and a subsequent wet etch of the oxide sub-layer can produce released, suspended structures. A SOI approach is especially prescribed when tight uniformity and dimension control is of concern. The single-crystalline silicon comprising the device layer offers excellent mechanical properties (including low intrinsic stress) over amorphous materials such as silicon nitride or polysilicon. Furthermore, single-crystal silicon has a low intrinsic mechanical loss, and from a material standpoint, it promises potential for high Q-factor devices [19]. Figure 2 clarifies the fabrication process detailed in this section.

SOI processing is not without its challenges and considerations, however. Given the requirement of perfectly smooth bonding surfaces during the formation of SOI wafers, one limitation on device dimensions and available process strategies is stiction [20], where the two highly defect-free surfaces permanently stick together after release [17]. The employed process mitigates this obstacle by establishing sub-surface parylene structures with a low-coefficient of friction that serve to interfere with the stiction process.

The device layer of the SOI wafer determines the thickness of the fabricated beam, with nominal $2\text{-}\mu\text{m}$ device and $5\text{-}\mu\text{m}$ buried-oxide layers to achieve the desired resonant frequency and spacing for the implemented electrostatic actuation mechanism. The silicon device layer supports a photolithographically defined PhC pattern that consists of shallow periodic holes imposed by an inductively-coupled plasma reactive-ion etch (ICP-RIE). This etch process transfers the PhC pattern

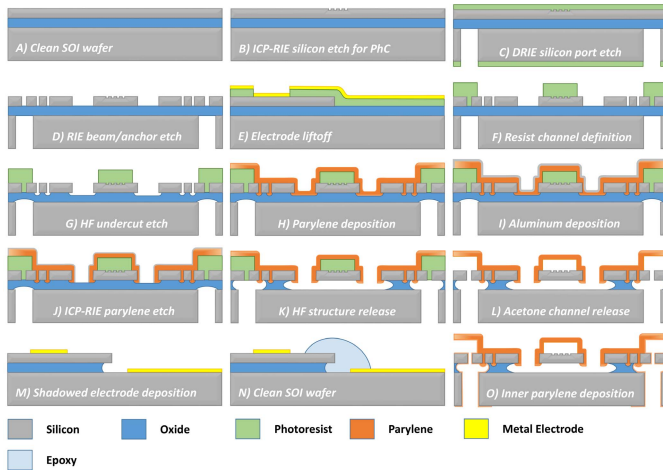


Fig. 2. Fabrication diagram (with illustrative scaling): (A) A clean SOI wafer. (B) An ICP-RIE silicon etch transfers the PhC pattern to the silicon device layer. (C) Both sides of the wafer are protected with photoresist, and a DRIE step etches port features. (D) A RIE process etches the silicon device layer to the oxide stop defining the resonator and parylene anchors. (E) A liftoff process deposits a metal electrode stack on the device layer. (F) Photolithography using a thick photoresist defines the device's channel structures. (G) A short HF etch of the oxide undercuts the silicon device layer to create anchor points for subsequent parylene processing. (H) A conformal parylene deposition encapsulates the photoresist and resonating structure. (I) A layer of aluminum is deposited over the structure as an etch mask. (J) An ICP-RIE etch through the parylene reveals the underlying oxide layer. (K) A HF wet etch fully undercuts and releases the structure to produce the freestanding resonator, and (L) the channel is released in acetone. (M) A shadow mask process deposits electrodes on the substrate. (N) Epoxy seals the undercut edges, and (O) a final parylene deposition electrically isolates the channel from the substrate.

into the silicon device layer with a vertical side-wall profile and a depth of about ~ 250 nm.

After establishment of the PhC, the frontside of the wafer was protected by a layer of photoresist, to reduce potential damage to the nanoscale optical structures and to serve as a safety barrier for through wafer etching. Photolithography defined a port pattern on the wafer's backside, and a deep reactive ion-etch (DRIE) etch opened fluidic passages through the backside of the wafer. By utilizing a Bosch process, the port-channels can be cleared through the wafer with good verticality, which is critical to the dimensions of the resulting frontside membrane. The insulating nature of the thick buried oxide ensures integrity of the frontside structures (by managing thermal stress) and accurately determines etch depth as a stop layer. The buried oxide then constitutes a surface, or membrane, on which sacrificial resist can be later spun and processed for channel formation. By way of the eventual HF release and resist scaffold, these ports subsequently connect to the frontside fluidic network, thereby allowing robust connection on the wafer's backside.

Anisotropic wet etching is another method for through wafer etching, using either potassium hydroxide (KOH) or tetramethylammonium hydroxide (TMAH) [21]. Wet etching can be significantly cheaper, especially given its suitability for batch processing; however, the required masking layers and mask etch selectivity rendered this method difficult to implement in the current process, requiring additional processing steps to

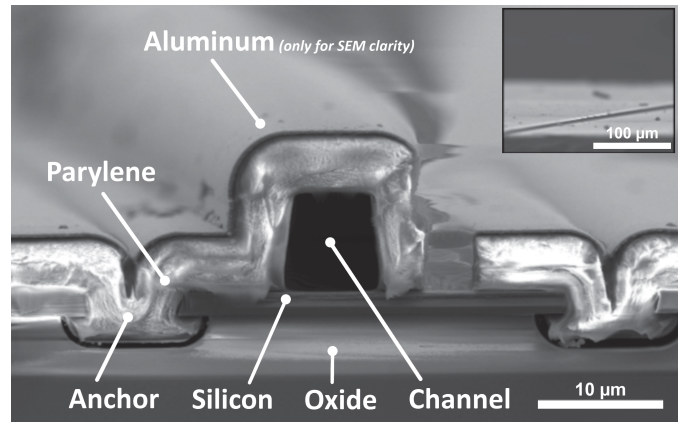


Fig. 3. SEM micrographs of the channel and its cross-section, identified by the released parylene structure and the adjacent anchors underlying the silicon device layer. Blanketing the parylene layer is a temporary aluminum film to provide electrical and thermal conduction for imaging.

remove the mask layer without affecting the supporting oxide membrane underlying the port structures. Further, the form that this composite silicon-silicon dioxide membrane takes is yet another deterring factor. The resulting structure must withstand many additional processing steps to become a permanent fixture in the fluidic channel. In addition to parylene integrity and attachment, this membrane has a limiting effect on the overall pressure allowed by the device. Therefore, careful design of this membrane is important to fluidic specifications, and a circular membrane demonstrates lower stress at its edges than rectangular or square membranes for a given pressure [22].

Following these steps was a reactive-ion etch (RIE), stopping on the buried oxide layer to define the beam structure and anchor sites, that facilitate later beam release and parylene deposition, respectively. While silicon serves as the structural, integrated-optical component, parylene-C confines fluid on the structure as the fluidic channel material. On its own, parylene-C typically has poor adhesion to other materials, including silicon, and cannot withstand severe or abrasive environments [23], rendering parylene a challenging material to process; however, its optical clarity and its dynamic scalability justify such added complexity, as scalability is a challenge for other standard-process, optically-clear materials. Other standard optically-viable materials that we considered were limited in their practical scalability and fabrication suitability.

A mitigating strategy propelled in this work to ensure reliable, robust fluidic channels, employs mechanical anchors below the silicon device layer for attachment of the parylene, which is important in determining the maximum fluidic pressure supported by the device and its reliability. The advantageous structure of the SOI wafer aids in construction of these anchors, whereas other published approaches utilized a modified Bosch process [24]. The buried oxide lends itself readily, where etching exposes the oxide and a timed hydrofluoric (HF) etch creates inverted mushroom-like cavities, without the need for implementing a more involved plasma etch process. Parylene then fills these voids to generate points of fixation for the layer, shown to the left and right of the channel in Fig. 3. This mechanical attachment is the most

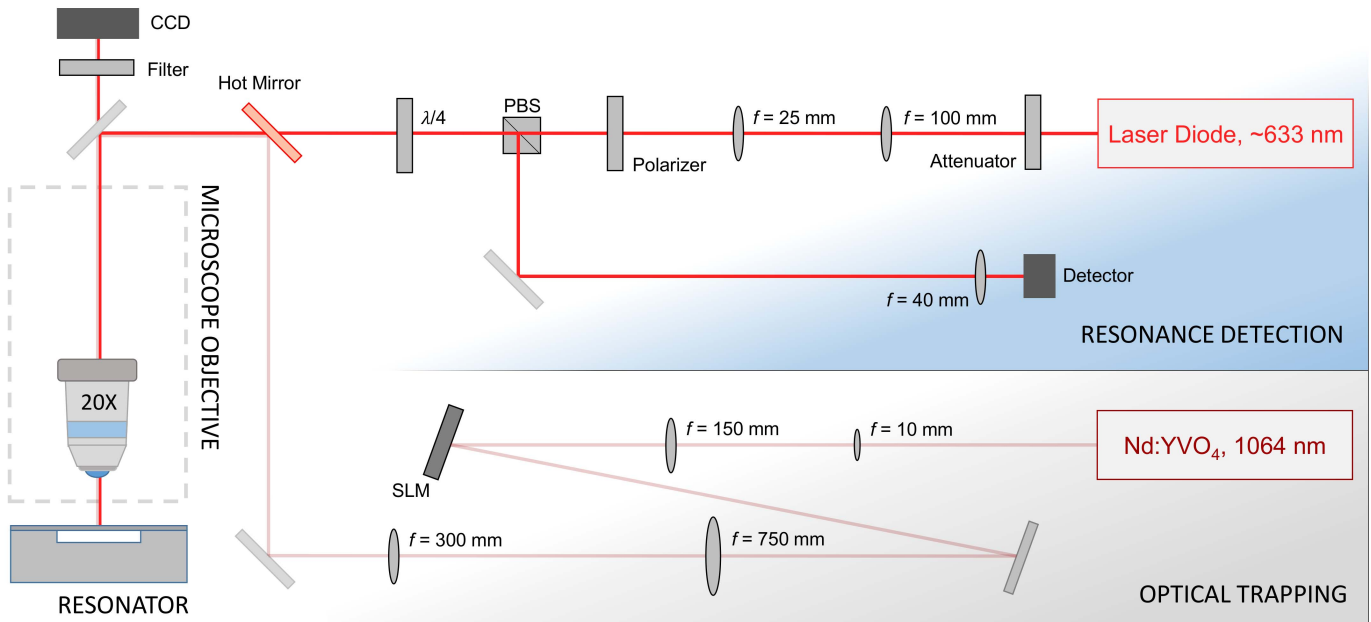


Fig. 4. Optical detection and laser trapping scheme showing a laser diode (for resonance detection) and a Nd:YVO₄ laser (for trapping) co-incident under microscope on the resonator device. A spatial light modulator (SLM) is included for holographic trapping capabilities.

vulnerable link in the fluidic structure, and therefore, becomes the determining factor in fluid pressure ratings for the device.

Parylene adhesion is not only a consideration for substrate attachment, but also affects subsequent processing steps. A layer of parylene can impair photoresist spinning, notably for severe surface topologies, and it has a comparably low thermal budget, prohibiting many etching and baking process steps. The addition of a patterned aluminum layer can help with some of these thermal issues as well as ensure sufficient masking on highly topological features, which can be later removed.

Before erecting the channel, a photolithography liftoff process created a metal electrode stack on the device, composed of chrome (~10 nm), nickel (~100 nm), and gold (~200 nm). Chrome served as an adhesion layer; nickel established a reinforced pad for better strength and durability during probing; and gold provided good conductivity.

Given a method of securing the parylene, channel formation required a sacrificial process. Such processing has seen important development [25]–[27] and serves as a key step in fabrication. Photoresist is easily patterned and readily dissolved in a host of solvents, and its cross-sectional profile can even be controlled through resist reflow [28]. To this end, patterned thick photoresist defined the height and width of the channel; as a result, these dimensions are easily adaptable to suit various application requirements and cell types. Upon establishing this layer, chemical-vapor-deposited parylene then coated the structure (~5 μm), encapsulating the beam resonator and the sacrificial photoresist, while simultaneously filling the cavity anchor sites for attachment. A long HF etch (~15 minutes) removed the supporting buried-oxide sublayer to fully release the beam-channel structure, followed by a final solvent release (>30 hours) of the sacrificial photoresist. Figure 3 shows a freestanding channel anchored in the oxide sublayer of a

SOI wafer; the top aluminum layer is for SEM clarity only, being removed later in the process. There is an optimization required during the HF etch step, one that minimizes etch time. The process has to ensure a long enough etch duration to fully release the structure; however, the longer the etch time, the deeper the adjacent substrate becomes undercut. This undesirable release leads to increased damping on the structure and an increase in effective structural mass, both detrimental effects in terms of frequency resolution and mass sensing. Therefore, careful etching is warranted for increased device performance.

As a final step, metal electrodes (gold pads, ~200 nm, with a chrome intermediate layer, ~10 nm) were deposited using a shadow mask to establish electrical contact with the substrate layer. By virtue of oxide undercutting and consequent separation, the substrate and device electrodes could be implicitly isolated. While convenient for electrode isolation, this overhanging edge could become very fragile depending on the extent of the undercut, and such fracturing can result in shorting. Careful selection of silicon doping impurities and bias polarity can reduce this shorting between the layers, and an encasing epoxy bead guarantees electrical and mechanical integrity for subsequent handling. More specific detail on this fabrication process can be found in [29].

III. EXPERIMENTAL SETUP

To implement both optical trapping and resonance detection, the system employed two independent lasers. Trapping and optical detection occur under microscope with 20–50X objective lenses, and the two beams were co-incident on the resonator through combination by a hot mirror, which transmitted visible wavelengths and reflected infrared (IR). The optical set-up is illustrated by Fig. 4, showing two separate

arms for resonance detection and optical trapping, in addition to the microscope.

A laser diode (<100 mW, nominally operated around 20 mW), temperature-controlled at 25°C by a thermoelectric cooler (TEC), served in the detection of the structure's resonant frequency. After collimation and attenuation (or control of the laser diode current), the setup utilized a linear polarizer, a quarter-waveplate ($\lambda/4$), and a polarizing-beam splitter (PBS) to maximize the intensity transmitted to the photodiode detector. By ensuring the correct orientation of linear polarization, most of the light was transmitted through the PBS to the waveplate, which then converted the laser's polarization to a circularly polarized beam. After undergoing reflection from the resonant structure and propagating in the opposite direction, the handedness of circular polarization rotated the output linear orientation by 90° to maximize light reflection at the PBS and intensity at the photodiode. This ensured a better signal-to-noise ratio (SNR) of the detected output. The large degree of diffraction from the PhC and the edges of the resonator were imaged onto the active region of the photodiode, and sensitive vibrational translations in the diffraction pattern drove modulation of the photodiode current to allow retrieval of the resonance signal.

The second sub-setup involved a Nd:YVO₄ laser (5 W, 1064 nm) to enable optical trapping (laser tweezers) for manipulation of cells and particles on the resonator. A series of collimating and magnifying lenses combined with a spatial light modulator (SLM) shaped and sized the trapping beam. The SLM could holographically create arbitrary beam patterns at the focal plane of the microscope to allow for additional functionality and adaptability of the implemented trapping approach. Once the beam reached the sample, it had an intensity on the order of $10^3 \mu\text{W}/\mu\text{m}^2$, depending on the utilized objective and laser current level.

Both lasers are introduced to the sample by a beam splitter adapted for both trapping and detection wavelengths. After collection by the objective lens, the light passes through a filter and is incident on a charge-coupled device (CCD) for digital image acquisition. The filter functions to reduce and block both lasers to maintain the microscope's imaging capability and to see both the location of the resonator and the samples undergoing measurement.

Attainment of a high-quality resonator is paramount in measuring the mass of single cells. As the most appropriate solution, we devised a specialized vacuum chamber (depicted in Fig. 5) that attached directly below the objective lens of the fluorescent microscope on a two-axis motorized stage. There were four external fluidic ports that allowed fluid to bypass the device. This is essential when loading the sample into the resonator; since the resonant channel is highly constricted to only sub-micro-liters of flow, it would be impractical to wait for macro-scale volumes of fluid to pass through the channel. Instead, the sample could be loaded by bypassing the device and continuing into a waste channel, as dictated by the pressure differential on all four ports.

The chamber allows device fluid connection from its bottom side with small O-ring seals that mate with etched port holes in the back of the silicon chip. A plate fastens over the device

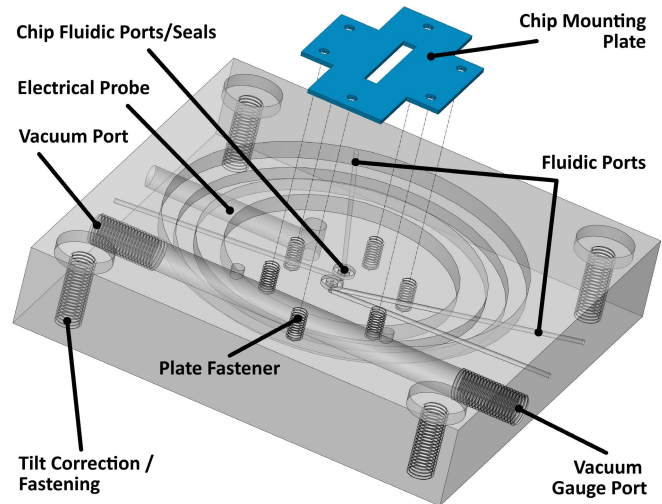


Fig. 5. A CAD model of the vacuum chamber mount, illustrating the chip mounting plate, and various ports for fluid, probing, and vacuum.

to ensure adequate compressive pressure to form a seal and fix device position. The plate has a slit opening to reveal the MEMS structure to the microscope and has six holes that mate with threading in the bottom of the chamber.

The larger port is dedicated to the electrical assembly, consisting of two wires to probe each electrode of the device. The ground electrode attaches to the mounting plate and contacts the substrate layer through gold pads deposited around the edges of the chip. The second wire forms a probe to connect the gold electrodes on the device layer surface. The electrodes are housed in a 1/8 NPT threaded fitting, which is sealed by a vacuum-grade epoxy.

There are four holes at each corner for securing the chamber that also serve as tilt-correction adjustments to ensure proper microscope alignment. The chamber itself was made of a polished acrylic plastic for two reasons: to create a chamber that was not conductive and would therefore not present additional challenges for probing the sample, and second, to achieve optical transparency, which yields tremendous aid in port alignment and monitoring the fluid lines for bubbles or other obstructions.

The chamber integrates two additional 1/8 NPT threaded holes: one connects to the vacuum pump and the other to a vacuum gauge for observation of chamber pressure. The chamber can achieve a vacuum level below 30 mTorr, and with a more powerful vacuum pump, this pressure may be further reduced. The vacuum chamber and the provided vacuum environment achieved at least a factor ten enhancement in Q-factor.

One practical challenge for chamber design was the close proximity between the device surface and the sealing window. Due to the short working distance of the microscope objective (~9 mm) and the existence of increased index of refraction in the beam path, the chamber had to possess a very shallow working depth, which did not allow for tall electrical probes or mounting structures. Therefore, window thickness and structure design were important for both spatial and optical-clarity considerations.

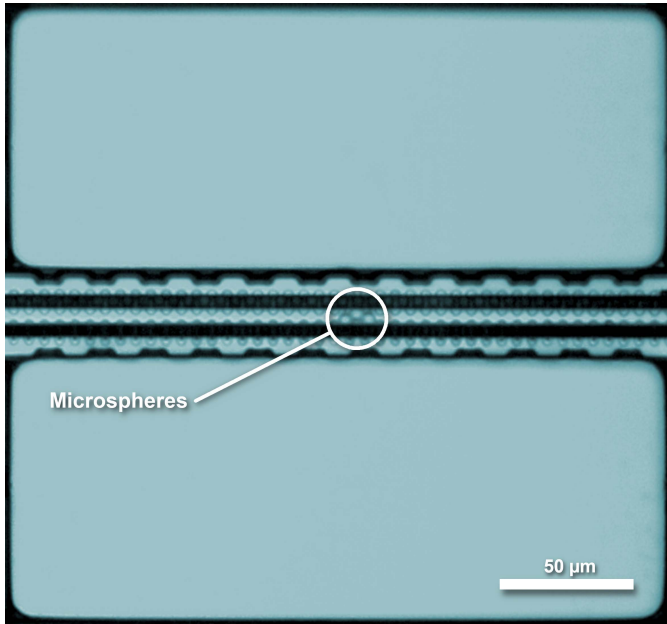


Fig. 6. Micrograph of the bridge resonator accompanied by three $5.5\text{-}\mu\text{m}$ polymer microspheres centered on the structure.

IV. OPTICAL CHARACTERIZATION

Upon refinement of the fabrication and set-up, we verified the optical compatibility of the parylene-silicon resonator. The first experiment sought particle positioning on the resonant structure. Figure 6 highlights three $5.5\text{-}\mu\text{m}$ polymer beads within the fluidic channel, clearly viewed by microscope. The figure illustrates good optical clarity within the channel, achieved by both the properties of the parylene and the geometry of the channel's apex. The optical path as it transitions from vacuum to parylene to fluid is governed by Snell's law, which becomes especially important if the channel assumes a large degree of curvature. Consequently, the fabrication process sought a flattened profile during sacrificial channel formation.

As introduced, optical trapping garners important attention in MEMS resonators for translational sensitivity dependence and long-term positioning. Speaking to this capacity, laser-tweezers experiments were conducted within the channel, depicted in Fig. 7(A), as the circled $1\text{-}\mu\text{m}$ polymer microsphere was moved along the channel, referenced to particles on the outside of the channel; its trajectory is shown by the dashed white line. The external particles (of larger size) were deposited and dried in-place by previous experiments, serving as a fixed reference. Additionally, the trapping laser was blocked by an optical filter to maintain sample visibility.

To demonstrate enabled fluorescent imaging through the transparent parylene-C layer, cadmium selenide (CdSe) quantum dots were loaded into the channel. The quantum dots fluoresce in the red wavelength band, which is clearly observed in Fig. 7(B). The quantum dots were distributed throughout the channel by their fluid suspension, and clearly highlight the interior volume of the channel and port structures. The blue features spur from diffraction of the stimulation wavelength, revealing the device's layout.

Through accommodation of these three optical characterization methods, the resonant mass sensor established its transparency and optical accessibility of measurement samples.

V. MASS MEASUREMENT

Measurement of mass is the second critical capability of the technology. Accordingly, two defining device characteristics are mass sensitivity and quality factor; sensitivity describes the resonator's frequency response to a given change in mass, i.e. how large is the expected shift upon adding mass, and the quality factor dictates the fidelity with which this resonant frequency shift can be determined. Sensitivity has a profound dependence on the overall mass of the MEMS structure itself, as we will visit further on.

To understand sensitivity for these devices, both measurement and finite-element-analysis (FEA) simulations (COMSOL Multiphysics® Structural Mechanics) revealed the structure's response with good agreement, as represented by Fig. 8. The simulation was based on Navier's equations; coupled with the appropriate fixed-fixed boundary conditions and an assumed harmonic solution, the eigenvalue problem was solved to reveal the natural frequency of the structure given various parameters including dimensions, material elasticity, temperature, loading, etc. The top surface describes sensitivity at the center of the structure, whereas the underlying surface represents that generated at the anchors where the resonator nominally fixes to the substrate. By maintaining optical availability of the channel contents, laser tweezers promises position control and therefore can minimize sensitivity variation (reducing mass measurement error) for the sample. This is especially important for long-term mass monitoring and for other resonator topologies that exhibit greater translational sensitivity dependence [12]. The simulation also shows an appreciable change in sensitivity for large sample mass. For small changes, device sensitivity can be linearly related to the ratio of resonant frequency to structural mass. As sample mass is increased, its own contribution to overall device mass non-intuitively reduces the solicited frequency change arising from a diminishing sensitivity.

The mass sensitivity was calibrated by measuring resonant frequency shifts induced by both known-density fluids (water and isopropanol) and standardized polymer beads (with $5.5\text{-}\mu\text{m}$ diameters and a density of 1.05 g/cm^3). In this way, the calibration considered particle mass ($\sim 100\text{ pg}$) up to fluid density changes ($\sim 10000\text{ pg}$). Since mass change shares a linear relationship with resonant frequency for relatively small changes in mass, the calibration is a simple ratio of resonant shift to mass change. As discussed, this ratio is dependent on position; therefore, to consider varying fluid density, which induces mass change distributed along the structure, the modal shape's influence on sensitivity must be considered by integrating its contribution along the length of the structure. The results from this analysis are shown in Fig. 8 as single calibration points, and the calibration method revealed a sensitivity of $\sim 1.2\text{ Hz/pg}$ at the center. Such a sensitivity is comparable to other similar-class sensors targeting cell applications, in the range of $0.8 \sim 1.4\text{ Hz/pg}$ [30].

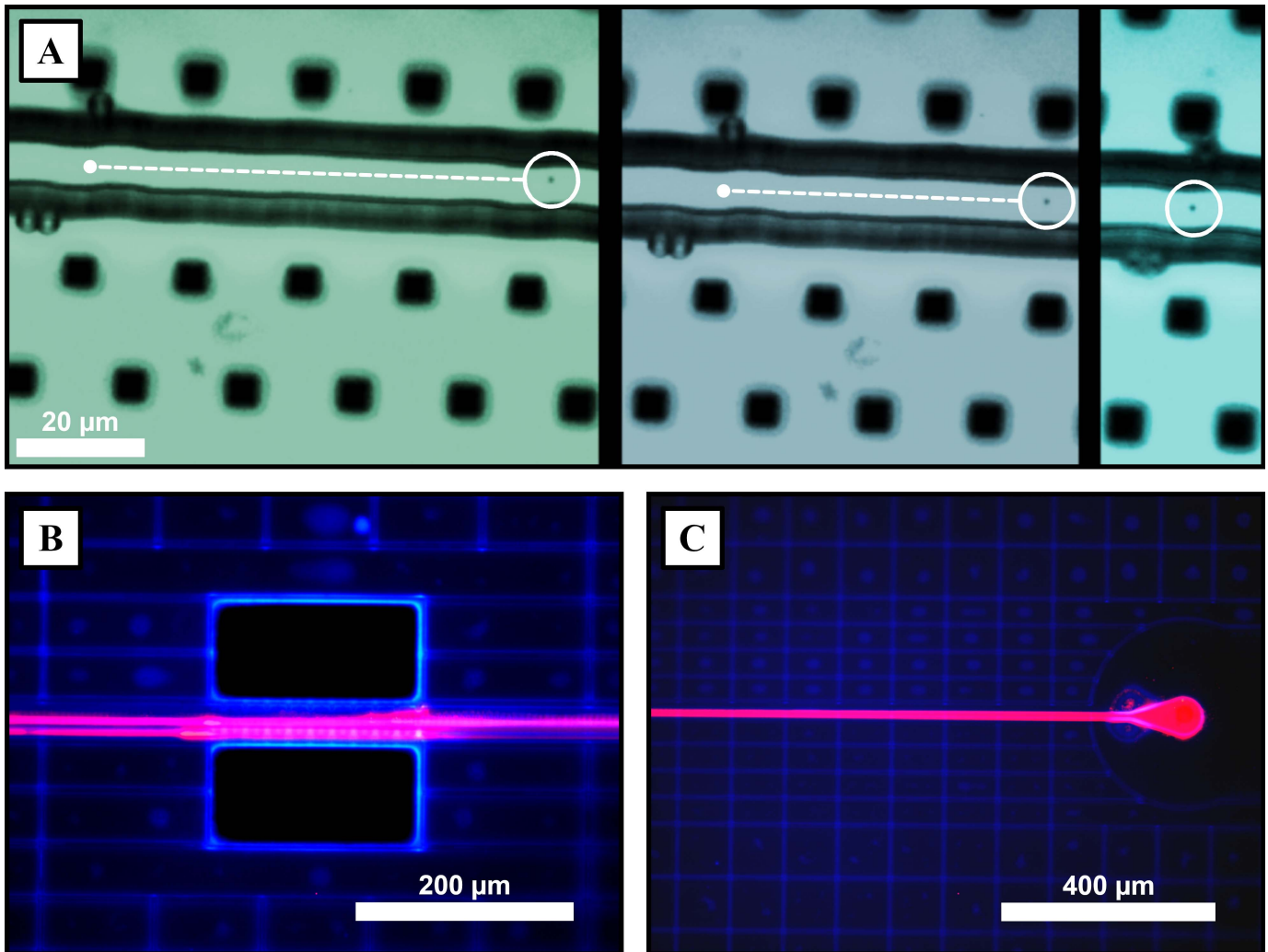


Fig. 7. (A) Sequential images showing a 1- μm polymer microsphere trapped within the channel's fluid volume and moved along the channel (the white dashed line represents its trajectory), relative to fixed particles external to the channel, residual from previous experiments. The trapping laser has been filtered for clarity. (B, C) Fluorescent micrographs of CdSe quantum dots exhibiting fluorescence and distributed within the fluidic channel, depicted in red. The blue excitation light is diffracted by device features and captured in the dark-field image. Both the bridge-resonator and channel port are depicted.

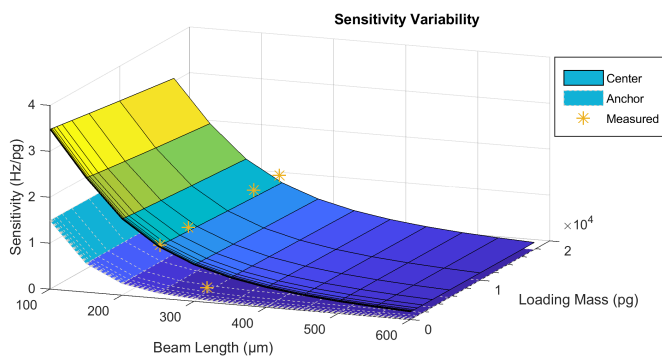


Fig. 8. Surface plots depicting sensitivity variation of structure mass, sample mass, and position (at its two boundary cases). The orange points indicate measured data and serve to unify simulation and measurement. Optical trapping can close the vertical gap in sensitivity, and structural design renders a device suitable for the appropriate mass responsivity.

In view of the quality factor, the device was electrostatically operated under feedback to monitor the resonant frequency and to ensure adequate frequency stability, as diagrammed

in Fig. 9(A) showing constituent components for detection, feedback, control, signal conditioning/protection, and data acquisition. In such a closed-loop topology, the MEMS resonator is the frequency-determining element in the subsequent oscillator, and the loop initializes through the detection of thermomechanical fluctuations in the beam. This signal is highly amplified and phase shifted by 90° , a condition for quality-factor enhancement, and the conditioned signal is then fed back to the resonator along with a bias voltage ($\sim 40\text{ V}$) to complete the loop. Given that the implementation is an unstable feedback loop and deflection amplitude stability is essential, the feedback gain is managed by a proportional-integral-derivative (PID) controller around some set point. This setup drives the structure to its natural resonant frequency with a fixed amplitude; in this way, the resonator is continuously driven at resonance with shifts arising from mass changes during measurement.

Well-tuned feedback ensures better overall frequency stability beyond that of the resonator itself. Fig. 9(B) shows a two-order magnitude improvement between direct

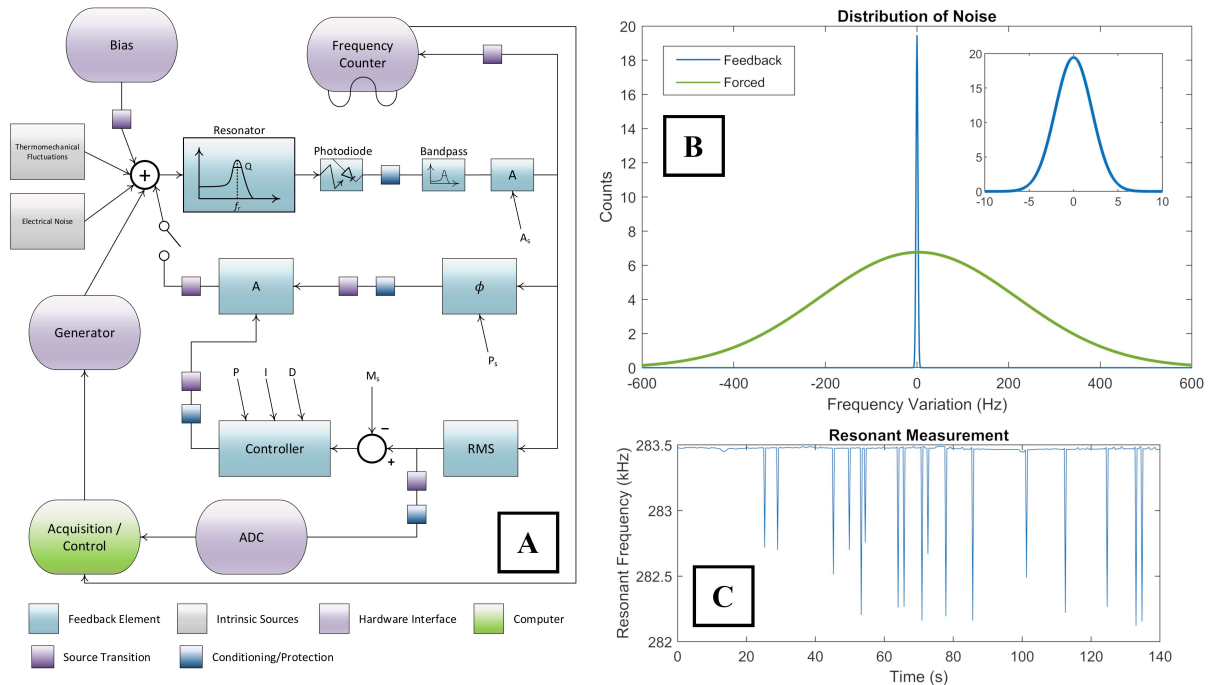


Fig. 9. (A) System block diagram comprising elements for detection, gain-controlled feedback drive, monitoring, and signal conditioning. (B) Feedback-drive improves frequency stability by two orders of magnitude when compared to direct drive. The inset figure shows an enlarged, detailed view of the response under feedback. (C) Real-time response from oil droplets (displacing water as a higher density medium) that create observable resonant-frequency downshifts.

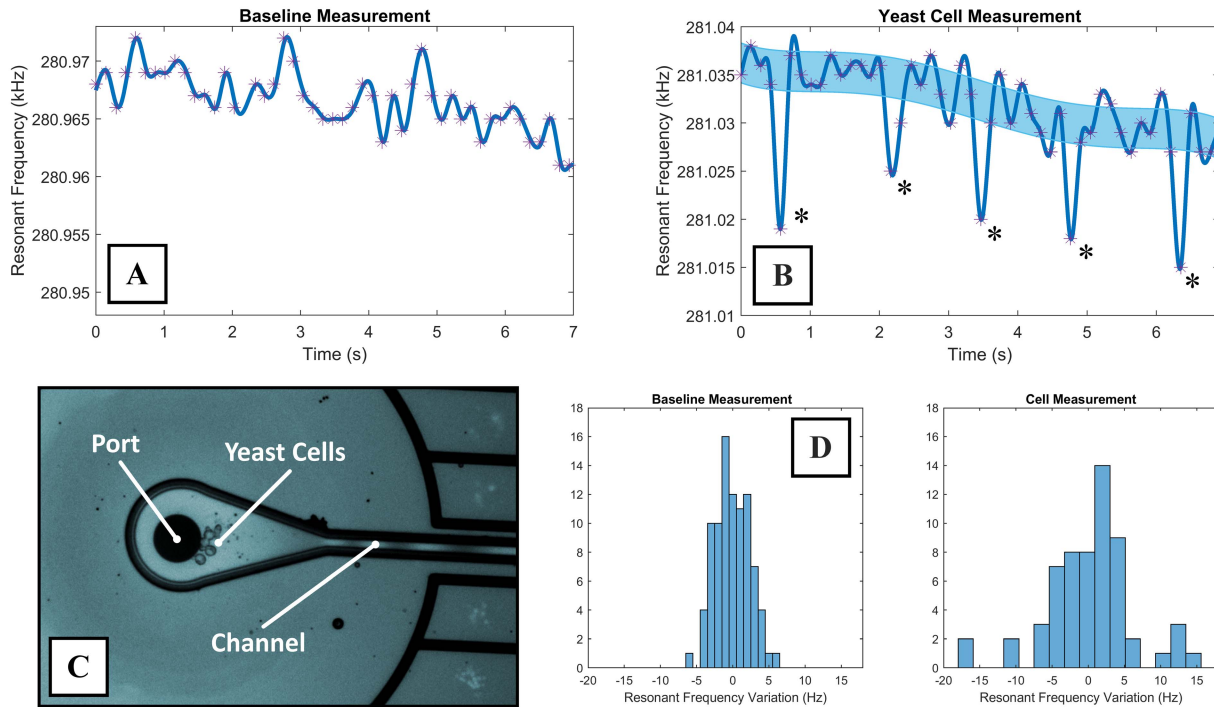


Fig. 10. (A) Resonant frequency data while passing only fluid through the channel. (B) Resonant frequency measurement of yeast cell clumps, identified by asterisks. The plot shows five clearly discernable frequency shifts in this particular data set. Single yeast cells were also measured, but they cannot be reliably separated from noise with statistical significance. (C) Micrograph of the device’s port and channel structures showing yeast cells queued in the channel, with a clear tendency to clump. (D) Histograms of resonant frequency variation with and without yeast cells to validate shifts arising from cell measurement.

and feedback drive approaches. With this system and its improved performance, real-time mass experiments showed rapid response to oil droplets (a denser medium than water) passing through the structure. This reaction to mass is indicated by the resonant frequency dips shown by Fig. 9(C).

Given fabricated devices and a tuned detection/feedback system, mass measurements were performed with cells. To this end, yeast cells were targeted due to their resiliency and simple culture protocol. For the experiment, a standard baker’s yeast strain (BY4741) was cultured on a solid agar plate at 30°C for

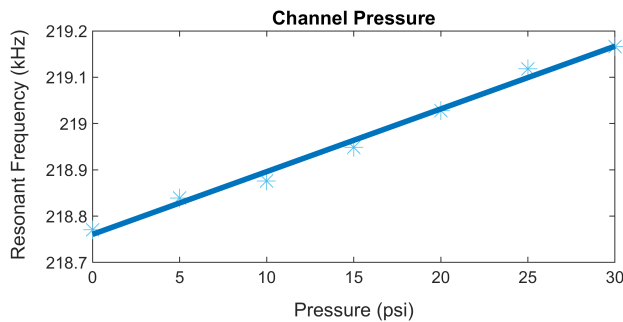


Fig. 11. Resonant frequency dependence on channel pressure fluctuation; a linear, direct relationship is clearly observed and is important to accurate mass measurement.

2 days, forming large ~ 1 mm colonies, and the cultured cells were then stored at 4°C . To prepare the cells for measurement, they were suspended and grown in a few milliliters of yeast extract peptone dextrose (YEPD).

The suspended-cell samples were injected into the device using the microfluidic pathways forged during fabrication, and the resonant frequency was monitored as they passed through the device channel. First, measurements were conducted on a channel passing only fluid, shown by Fig. 10(A) to achieve a baseline result. Subsequently, the response of the device to passing yeast cells is shown in Fig. 10(B); the light blue region of the plot indicates the level of frequency jitter that was present in Fig. 10(A), on the level of a few Hertz. In executing the calibration of these devices, we also considered the resonator's response to external factors, including channel pressure, bias voltage, surrounding vacuum pressure, and localized temperature effects. Given these findings and the experiments of interest, we concluded that the data exhibited drift primarily dominated by pressure fluctuations within the channel. This drift was then fitted as the global signal trend and used as a reference against the more rapid frequency shifts for cell mass determination. To further substantiate these pressure influences, Fig. 11 shows the resonant frequency response to variation in differential pressure across the channel. This observed relationship indicates the importance of careful fluidic control to minimize pressure fluctuations when retrieving viable sensor data.

Out of this frequency variability are clear dips in resonance frequency that indicate cell passage over the structure. The shifts represent the additive mass of multiple cells, owed to yeast's tendency to clump and bud, especially when confined into narrow fluidic pathways. This clumping nature is shown more clearly in Fig. 10(C) where cells are queued up for measurement in the port/channel. It is also important to note that the budding yeast were not synchronized in their cell cycle, and were therefore likely to present a wide range of cell sizes and states. Finally, Fig. 10(D) contrasts the resonant frequency variation in both the baseline and cell measurements to validate the observation of shifts arising from cell passage. Each dip in Fig. 10(B) represents a mass change of $8 \sim 14$ pg according to calibrated sensitivity with an average value of 11 pg. From the literature, yeast cells have

been shown to range in mass from $4 \sim 10$ pg as they undergo their cell cycle [31], and comparison with prior studies gives credibility to the result shown in Fig. 10.

VI. CONCLUSION

This work presents an optically viable MEMS-microfluidic sensor that serves as both a platform for mass measurement and optical characterization and control, enabling simultaneous application for two powerful classes of technologies. Aside from having enough sensitivity and scalability for experiments involving cells, the device features optical compatibility with a number of optical/near-infrared techniques, including fluorescence imaging, optical trapping, and flow cytometry, and consequentially, cells can be fully monitored/characterized as they undergo mass measurement. This technology unification is a first of its kind, and future avenues could employ this union in characterizing, simultaneously and with high accuracy, both mass accumulation and fluorescence-expressed cell dynamics in furtherance of human disease understanding, its treatment, and fundamental biological discovery. Proficiency on the level of discreet cells has especially important implications for both general biology and medicine as researchers continue to develop lab-on-chip platforms for accelerated therapeutic development and engineering of tissues and medical devices.

ACKNOWLEDGMENT

Device fabrication occurred in the Washington Nanofabrication Facility (WNF) and characterization in the Molecular Analysis Facility (MAF) at the University of Washington. We would like to acknowledge Arvind Subramaniam and Heungwon Park, from the Fred Hutchinson Cancer Research Center, for contributing cell strains and valuable guidance to this work.

REFERENCES

- [1] M. A. Mansor and M. R. Ahmad, "Single cell electrical characterization techniques," *Int. J. Mol. Sci.*, vol. 16, no. 6, pp. 12686–12712, Jun. 2015.
- [2] G. Popescu, K. Park, M. Mirac, and R. Bashir, "New technologies for measuring single cell mass," *Lab Chip*, vol. 14, no. 4, pp. 646–652, 2014.
- [3] K. G. Phillips *et al.*, "Optical quantification of cellular mass, volume, and density of circulating tumor cells identified in an ovarian cancer patient," *Frontiers Oncol.*, vol. 2, p. 72, Jul. 2012.
- [4] M. Koch, A. G. R. Evans, and A. Brunnschweiler, "Design and fabrication of a micromachined Coulter counter," *J. Micromech. Microeng.*, vol. 9, no. 2, pp. 159–161, 1999.
- [5] T. A. Zangle and M. A. Teitell, "Live-cell mass profiling: An emerging approach in quantitative biophysics," *Nature Methods*, vol. 11, no. 12, pp. 1221–1228, Dec. 2014.
- [6] H. Baltes and O. Brand, "CMOS-based microsensors and packaging," *Sens. Actuators A, Phys.*, vol. 92, nos. 1–3, pp. 1–9, Aug. 2001.
- [7] K. Park *et al.*, "Measurement of adherent cell mass and growth," *Proc. Nat. Acad. Sci. USA*, vol. 107, no. 48, pp. 20691–20696, Nov. 2010.
- [8] T. P. Burg *et al.*, "Weighing of biomolecules, single cells and single nanoparticles in fluid," *Nature*, vol. 446, no. 7139, pp. 1066–1069, Apr. 2007.
- [9] A. K. Bryan, V. C. Hecht, W. Shen, K. Payer, W. H. Grover, and S. R. Manalis, "Measuring single cell mass, volume, and density with dual suspended microchannel resonators," *Lab Chip*, vol. 14, no. 3, pp. 569–576, Feb. 2014.
- [10] M. M. Stevens *et al.*, "Drug sensitivity of single cancer cells is predicted by changes in mass accumulation rate," *Nature Biotechnol.*, vol. 34, no. 11, pp. 1161–1167, Oct. 2016.

- [11] Y. Weng, F. F. Delgado, S. Son, T. P. Burg, S. C. Wasserman, and S. R. Manalis, "Mass sensors with mechanical traps for weighing single cells in different fluids," *Lab Chip*, vol. 11, no. 24, pp. 4174–4180, Oct. 2011.
- [12] E. G. Keeler, P. Jing, J. Wu, C. Zou, and L. Y. Lin, "MEMS resonant mass sensor with integrated optical manipulation," *IEEE Trans. Nanotechnol.*, vol. 17, no. 4, pp. 714–718, Jul. 2018.
- [13] T. P. Burg *et al.*, "Vacuum-packaged suspended microchannel resonant mass sensor for biomolecular detection," *J. Microelectromech. Syst.*, vol. 15, no. 6, pp. 1466–1476, Dec. 2006.
- [14] T. P. Burg and S. R. Manalis, "Suspended microchannel resonators for biomolecular detection," *Appl. Phys. Lett.*, vol. 83, no. 13, pp. 2698–2700, Sep. 2003.
- [15] P. Jing, J. Wu, G. W. Liu, E. G. Keeler, S. H. Pun, and L. Y. Lin, "Photonic crystal optical tweezers with high efficiency for live biological samples and viability characterization," *Sci. Rep.*, vol. 6, Jan. 2016, Art. no. 19924.
- [16] B. H. Kim, D. P. Kern, S. Raible, and U. Weimar, "Fabrication of micro-mechanical mass-sensitive resonators with increased mass resolution using SOI substrate," *Microelectron. Eng.*, vols. 61–62, pp. 947–953, Jul. 2002.
- [17] J. Kiihamäki, J. Dekker, P. Pekko, H. Kattelus, T. Sillanpää, and T. Mattila, "'Plug-up'—A new concept for fabricating SOI MEMS devices," *Microsyst. Technol.*, vol. 10, no. 5, pp. 346–350, Aug. 2004.
- [18] K. Yoshimoto, R. Suzuki, Y. Ishikawa, and K. Wada, "Bandgap control using strained beam structures for Si photonic devices," *Opt. Express*, vol. 18, no. 25, pp. 26492–26498, Dec. 2010.
- [19] E. Serra, M. Bonaldi, A. Borrielli, L. Conti, G. Pandraud, and P. M. Sarro, "Low loss single-crystal silicon mechanical resonators for the investigation of thermal noise statistical properties," *Sens. Actuators A, Phys.*, vol. 227, pp. 48–54, May 2015.
- [20] Z. Yapu, "Stiction and anti-stiction in MEMS and NEMS," *Acta Mech. Sinica*, vol. 19, no. 1, pp. 1–10, Feb. 2003.
- [21] M. Shikida, K. Sato, K. Tokoro, and D. Uchikawa, "Differences in anisotropic etching properties of KOH and TMAH solutions," *Sens. Actuators A, Phys.*, vol. 80, no. 2, pp. 179–188, Mar. 2000.
- [22] R. Khakpour, S. R. M. Mansouri, and A. R. Bahadorimehr, "Analytical comparison for square, rectangular and circular diaphragms in MEMS applications," in *Proc. Int. Conf. Electron. Devices, Syst. Appl. (ICEDSA)*, Kuala Lumpur, Malaysia, Apr. 2010, pp. 297–299.
- [23] J. Charmet, J. Bitterli, O. Sereda, M. Liley, P. Renaud, and H. Keppner, "Optimizing Parylene C adhesion for MEMS processes: Potassium hydroxide wet etching," *J. Microelectromech. Syst.*, vol. 22, no. 4, pp. 855–864, Aug. 2013.
- [24] Q. He, E. Meng, Y.-C. Tai, C. M. Rutherglen, J. Erickson, and J. Pine, "Parylene neuro-cages for live neural networks study," in *12th Int. Conf. Solid-State Sens., Actuators Microsyst. Dig. Tech. Papers (TRANSDUCERS)*, Boston, MA, USA, Jun. 2003, pp. 995–998.
- [25] K. Walsh, J. Norville, and Y.-C. Tai, "Photoresist as a sacrificial layer by dissolution in acetone," in *IEEE 14th Int. Conf. Micro Electro Mech. Syst. Tech. Dig. (MEMS)*, Interlaken, Switzerland, Jan. 2001, pp. 114–117.
- [26] B. A. Peeni, M. L. Lee, A. R. Hawkins, and A. T. Woolley, "Sacrificial layer microfluidic device fabrication methods," *Electrophoresis*, vol. 27, no. 24, pp. 4888–4895, Dec. 2006.
- [27] J. R. Lee, J. P. Barber, Z. A. George, M. L. Lee, H. Schmidt, and A. R. Hawkins, "Microchannels with rectangular and arched core shapes fabricated using sacrificial etching," *J. Micro/Nanolithography, MEMS, MOEMS*, vol. 6, no. 1, Jan. 2007, Art. no. 013010.
- [28] C.-T. Seo, C.-H. Bae, D.-S. Eun, J.-K. Shin, and J.-H. Lee, "Fabrication of circular-type microchannel using photoresist reflow and isotropic etching for microfluidic devices," *Jpn. J. Appl. Phys.*, vol. 43, no. 11A, pp. 7773–7776, Nov. 2004.
- [29] E. G. Keeler, "MEMS resonant mass sensing with enabled optical interaction for cellular study," Ph.D. dissertation, Dept. Elect. Comput. Eng., Univ. Washington, Seattle, WA, USA, 2018.
- [30] N. Cermak *et al.*, "High-throughput measurement of single-cell growth rates using serial microfluidic mass sensor arrays," *Nature Biotechnol.*, vol. 34, no. 10, pp. 1052–1059, Oct. 2016.
- [31] A. K. Bryan, A. Goranov, A. Amon, and S. R. Manalis, "Measurement of mass, density, and volume during the cell cycle of yeast," *Proc. Nat. Acad. Sci. USA*, vol. 107, no. 3, pp. 999–1004, Jan. 2010.

Authors' photographs and biographies not available at the time of publication.